University of Texas Rio Grande Valley

# ScholarWorks @ UTRGV

Biology Faculty Publications and Presentations                    College of Sciences

3-2021

# Mitochondrial OPA1 cleavage is reversibly activated by differentiation of H9c2 cardiomyoblasts

Iraselia Garcia
*The University of Texas Rio Grande Valley*

Fredy Calderon
*The University of Texas Rio Grande Valley*

Patrick De la Torre
*The University of Texas Rio Grande Valley*

Shaynah St. Vallier
*The University of Texas Rio Grande Valley*

Cristobal Rodriguez
*The University of Texas Rio Grande Valley*

*See next page for additional authors*

## Recommended Citation

Garcia, I., Calderon, F., la Torre, P. D., Vallier, S. St., Rodriguez, C., Agarwala, D., Keniry, M., Innis-Whitehouse, W., & Gilkerson, R. (2021). Mitochondrial OPA1 cleavage is reversibly activated by differentiation of H9c2 cardiomyoblasts. Mitochondrion, 57, 88–96. https://doi.org/10.1016/j.mito.2020.12.007

## Authors

Iraselia Garcia, Fredy Calderon, Patrick De la Torre, Shaynah St. Vallier, Cristobal Rodriguez, Divya Agarwala, Megan Keniry, Wendy Innis-Whitehouse, and Robert Gilkerson
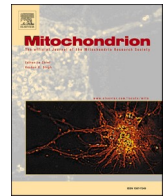
# Mitochondrial OPA1 cleavage is reversibly activated by differentiation of H9c2 cardiomyoblasts

Iraselia Garcia [a,b], Fredy Calderon [a], Patrick De la Torre [a], Shaynah St. Vallier [a], Cristobal Rodriguez [a], Divya Agarwala [a], Megan Keniry [a], Wendy Innis-Whitehouse [c], Robert Gilkerson [a,d,*]

[a] *Department of Biology, The University of Texas Rio Grande Valley, Edinburg, TX, USA*
[b] *Department of Biology, South Texas College, McAllen, TX, USA*
[c] *Biomedical Sciences, The University of Texas Rio Grande Valley, Edinburg, TX, USA*
[d] *Clinical Laboratory Sciences, The University of Texas Rio Grande Valley, Edinburg, TX, USA*

## ARTICLE INFO

## ABSTRACT

Optic atrophy-1 (OPA1) is a dynamin-like GTPase localized to the mitochondrial inner membrane, playing key roles in inner membrane fusion and cristae maintenance. OPA1 is regulated by the mitochondrial transmembrane potential ($\Delta\psi_m$): when $\Delta\psi_m$ is intact, long OPA1 isoforms (L-OPA1) carry out inner membrane fusion. Upon loss of $\Delta\psi_m$, L-OPA1 isoforms are proteolytically cleaved to short (S-OPA1) isoforms by the stress-inducible OMA1 metalloprotease, causing collapse of the mitochondrial network and promoting apoptosis. Here, we show that L-OPA1 isoforms of H9c2 cardiomyoblasts are retained under loss of $\Delta\psi_m$, despite the presence of OMA1. However, when H9c2s are differentiated to a more cardiac-like phenotype via treatment with retinoic acid (RA) in low serum media, loss of $\Delta\psi_m$ induces robust, and reversible, cleavage of L-OPA1 and subsequent OMA1 degradation. These findings indicate that a potent developmental switch regulates $\Delta\psi_m$-sensitive OPA1 cleavage, suggesting novel developmental and regulatory mechanisms for OPA1 homeostasis.

## 1. Introduction

Mammalian OPA1 is localized to the mitochondrial inner membrane, playing a key role in coordinating mitochondrial structure, bioenergetics, and stress response. Expressed as 8 different mRNAs due to variable splicing (Delettre et al., 2001; Olichon et al., 2007; Akepati et al., 2008), mitochondrial OPA1 is present as five distinct protein isoforms. Two long (L-OPA1) isoforms can be cleaved at either the S1 or S2 sites to generate three short S-OPA1 isoforms (Griparic et al., 2007). L-OPA1 mediates inner membrane fusion (Song et al., 2007; Baricault et al., 2007), either by binding cardiolipin or through homodimeric association (Ban et al., 2017), while S-OPA1 isoforms are released into the intermembrane space and are fusion-inactive (Song et al., 2007; Ishihara et al., 2006). Loss of L-OPA1 and accumulation of S-OPA1 promotes apoptosis (Head et al., 2009; Jiang et al., 2014) and autophagy

(Chen et al., 2016). Consistent with this, increased expression of OPA1 confers protection against apoptotic stimuli (Civiletto et al., 2015; Merkwirth et al., 2008), while loss of OPA1 expression sensitizes cells to apoptosis (Frezza et al., 2006); demonstrating the importance of OPA1 to mitochondrial structure/function homeostasis and cellular stress response.

L-OPA1 isoforms are cooperatively cleaved by the inner membrane proteases YME1L and OMA1 (Anand et al., 2014). YME1L constitutively cleaves L-OPA1 for steady-state levels of S-OPA1 (Griparic et al., 2007; Guillery et al., 2008), while OMA1 cleaves L-OPA1 in response to loss of transmembrane potential across the inner membrane ($\Delta\psi_m$) (Head et al., 2009; Ehses et al., 2009) as an inducible protease activated by a range of stress stimuli (Rainbolt et al., 2016). Following import to the mitochondria, OMA1 is cleaved to a mature form by AFG3L2 (Consolato et al., 2018). In response to loss of $\Delta\psi_m$, OMA1 cleaves L-OPA1 and then

undergoes self-cleavage (Zhang et al., 2014) in a YME1L-dependent manner (Rainbolt et al., 2016). The activation of OMA1 in response to loss of $\Delta\psi_m$ requires the matrix-oriented N-terminal domain of OMA1 (Baker et al., 2014); however, the underlying mechanism of stress-sensitive OMA1 activation remains unclear.

Consistent with OPA1's roles in mitochondrial homeostasis and apoptotic induction, recent work suggests that OPA1 has broad importance in cellular development and differentiation. Mitochondrial fusion is mechanistically involved in cell cycle progression (Mitra et al., 2009), with OPA1 specifically required for maintenance of germline stem cells (Sênos Demarco et al., 2019) and developmental angiogenesis (Herkenne et al., 2020). OPA1 expression is upregulated during cardiac differentiation of stem cells (Magalhães-Novais et al., 2020), while disruption of OPA1 prevents cardiomyocyte differentiation (Kasahara et al., 2013), suggesting a key role for OPA1 in cardiac development. Despite the emerging importance of OPA1, however, developmental regulation of $\Delta\psi_m$-sensitive OPA1 cleavage has not been reported. Previously, we found that OMA1 controls a sharply-defined threshold of $\Delta\psi_m$ required for OPA1-mediated mitochondrial fusion in 143B osteosarcoma cells (Jones et al., 2017). In exploring whether a similar threshold might exist in H9c2 cardiomyoblasts, we find that L-OPA1 is retained despite loss of $\Delta\psi_m$, but that $\Delta\psi_m$-sensitive L-OPA1 cleavage is fully and reversibly activated by retinoic acid (RA)-mediated differentiation. These findings indicate that a novel developmental switch potently activates $\Delta\psi_m$-sensitive OPA1 cleavage, raising exciting new questions regarding the underlying mechanisms and developmental roles of OPA1-mediated mitochondrial stress response.

## 2. Methods

### 2.1. Cell culture

H9c2 cardiomyoblasts from *R. norvegicus* (ATCC CRL-1446), 143B osteosarcomas, and *OMA1*+/+ and −/− mouse embryonic fibroblasts, were grown in Gibco Dulbecco's Modified Eagle's Medium (with high glucose, L-glutamine, phenol red, and sodium pyruvate) supplemented with 10% fetal bovine serum and Gibco antibiotic/antimycotic in 5% $CO_2$ at 37 °C. For carbonyl cyanide chlorophenyl hydrazone (CCCP) treatments, CCCP (Sigma) was added to media from 1 mM stock in DMSO for indicated times and concentrations. Differentiation of H9c2s was performed using the method of Branco et al. (2015): 350,000 cells were plated per 10 cm dish in DMEM + 10% FBS. The following day, differentiation was initiated by replacing the media with DMEM + 1% FBS + 1 μM RA (Sigma, from 1 mM stock in DMSO). RA-mediated differentiation proceeded for 5 days, with media changed every day. For undifferentiated controls, 50,000 cells were plated per 10 cm dish in DMEM + 10% FBS and grown alongside for 5 days. For galactose experiments, cells were grown in DMEM lacking glucose (Gibco 11966025) supplemented with sodium pyruvate and galactose with 10% FBS for three passages prior to lysate preparation.

### 2.2. Confocal imaging and analysis

For immunofluorescence microscopy (Fig. 1), cultured cells grown on 22 × 22 mm glass coverslips in 6-well culture dishes were washed briefly with PBS and fixed with 4% paraformaldehyde (Electron Microscopy Sciences, Hatfield, PA) and permeabilized with 0.1% TX-100 in
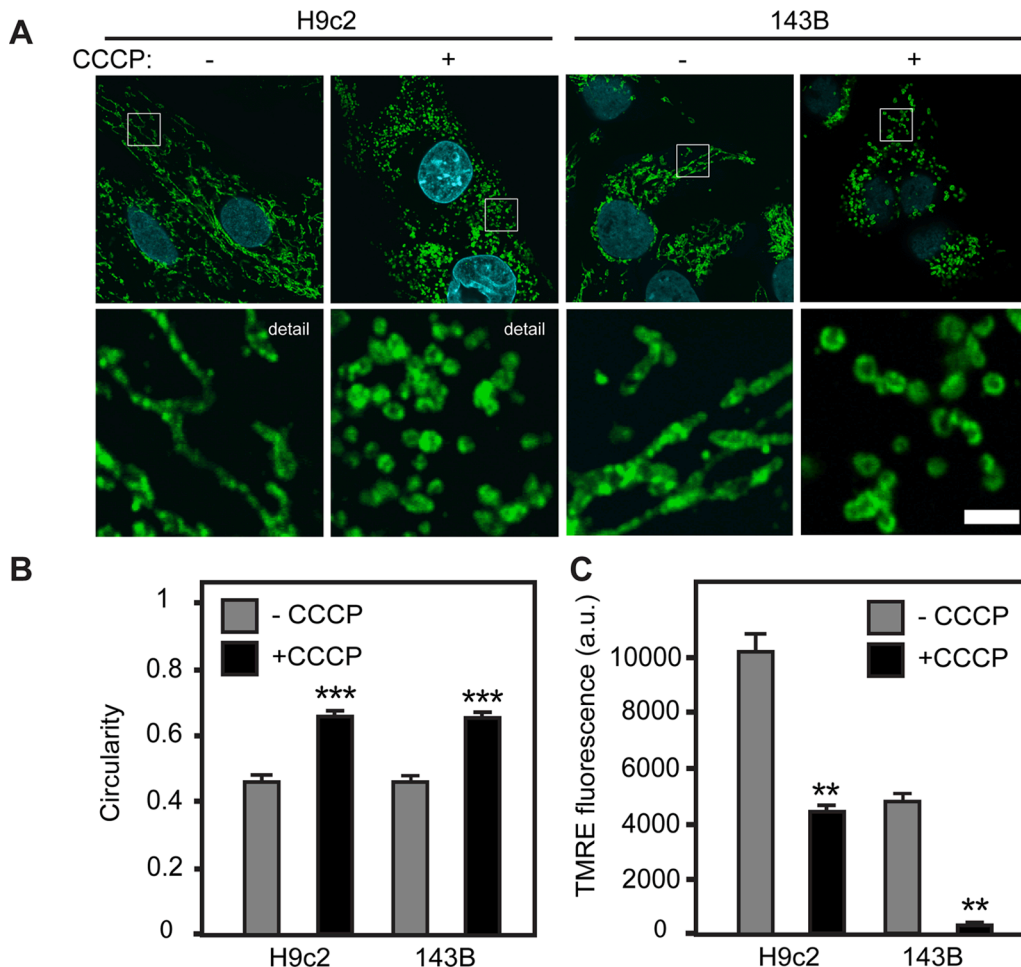
**Fig. 1.** Loss of $\Delta\psi_m$ causes fragmentation of the mitochondrial network. A. Confocal microscopy of H9c2 and 143B cells without or with CCCP treatment (10 μM, 1 h) immunolabeled for mitochondrial TOM 20 (green). Nuclei stained with DAPI (cyan). n = 3 experiments (biological replicates). Size bar = 2 μm. B. ImageJ quantification of mitochondrial circularity calculated from confocal images (detail) in A. n = 25 images for each, ± standard error. *** denotes p < 0.001. C. TMRE flow cytometry of H9c2 and 143B cells without or with CCCP, 10 μM, 1 h. n ≥ 3 experiments, ± standard error. ** denotes p < 0.01.

PBS for 10 min. Samples were blocked with 10% normal goat serum and immunolabeled with anti-TOM20 rabbit polyclonal antibody (FL-145, Santa Cruz Biotechnology, Santa Cruz, CA) at 1:100 dilution in PBS (note: antibody FL-145 is no longer available; the replacement, FL-10, reacts with human but not rat). Coverslips were washed briefly with PBS and incubated with goat anti-mouse AlexaFluor488 (Invitrogen Molecular Probes, Carlsbad, CA), followed by staining with diaminophenylindole (DAPI) to visualize cell nuclei, washed with PBS, and mounted in 50% glycerol in PBS. For imaging of differentiated H9c2 cell morphology (Fig. 3A), cells were fixed in 4% paraformaldehyde, washed briefly, and incubated with AlexaFluor488 phalloidin (Invitrogen Molecular Probes) and DAPI, as above. Coverslips were visualized on an Olympus Fluoview FV10i confocal microscope (Olympus, Waltham, MA) using a 60x objective (UPLSA60x W, aperture 1.0, 3.0 optical zoom). To quantify mitochondrial circularity, blinded ImageJ analysis was used as previously (Dagda et al., 2009; Garcia et al., 2018): microscopy samples were prepared and imaged with generic labeling, generating a sample size of n = 25 high resolution images for analysis. For each high resolution image (examples: Fig. 1A, detail images), ImageJ calculated the average circularity of the mitochondrial profiles in that image using the ImageJ Mitochondrial Morphology macro (http://imagejdocu.tudor.lu/doku.php?id=plugin:morphology:mitochondrial_morphology_macro_plug-in:start). To monitor mitochondrial morphology (Fig. 3F), RA-treated H9c2s were labeled with 40 nM MitoTracker Red CMXRos (Invitrogen Molecular Probes, Eugene, Oregon) for 20 min. followed by incubation in media lacking or containing 10 μM CCCP for 1 h, fixation in 4% paraformaldehyde for 30 min., and mounting/visualization.

### 2.3. Immunoblotting

For SDS-PAGE Western blotting, cells on 10 cm dishes were lysed in Laemmli buffer with β-mercaptoethanol (Bio-Rad). Equal volumes of cell lysates were electrophoresed through 6% (for OPA1), 10% (for OMA1), or 10–20% (for all others) acrylamide gels and transferred to Immobilon PVDF (Bio-Rad). For cellular fractionation to obtain cytosolic and crude mitochondrial fractions, 4–6 10 cm dishes of actively-dividing H9c2s were pooled and processed using the Mitochondria Isolation Kit for Cultured Cells (ThermoFisher 89874), and mitochondrial pellets resuspended in 1% CHAPS in TBS. Protein concentration of cytosolic and mitochondrial fractions were measured by $A_{280}$ using a NanoDrop spectrophotometer. 10 μg of protein were resuspended in Laemmli buffer with β-mercaptoethanol, electrophoresed on a 10% polyacrylamide gel and transferred to PVDF. Membranes were blocked with 5% nonfat milk in Tris-buffered saline + Tween (TBST). Primary antibody incubations were: OPA1 (BD Biosci. 612606) 1:500 overnight at 4 °C, OMA1 (Santa Cruz, H-11 sc-515788), 1:200 overnight at 4 °C, tubulin (Sigma, T6074) 1:1000 1 h, AFG3L2 (Invitrogen, PA5-48533) 1:1000, Bax (Cell Signaling, 2272) 1:1000 overnight 4 °C, VDAC (Abcam ab14734) 1 mg/mL, YME1L (Abgent AP4882a) 1:1000. Membranes were incubated with secondary goat anti-mouse poly-HRP (Invitrogen, 32230) or goat anti-rabbit poly-HRP at 1:3000 dilution for 1 h, washed, and developed using WestDura SuperSignal (Thermo, 34076). OMA1 blots required a high salt wash (1 g NaCl in 50 mL TBST) prior to developing. Blots were visualized using a GelDoc XR + Gel Documentation System (Bio-Rad). Each blot shown in a figure is representative of results obtained in at least three independent biological replicates. Similarly, ImageJ quantitation of immunoblots was performed on at least three independent biological replicates in all cases.

### 2.4. Flow cytometry

To monitor $\Delta\psi_m$, TMRE flow cytometry was used as previously (Jones et al., 2017; Garcia et al., 2018). Cells in 10 cm dishes were incubated with 100 nM tetramethyl rhodamine ester (TMRE, Invitrogen) in fresh media for 20 min, washed twice with PBS, and resuspended in 1 mL of PBS. Cells were analyzed on a BD FACSCelesta or LSR Fortessa (BD Biosciences). All flow cytometry graphs indicate the average peak fluorescence value and standard error of at least three independent biological replicates.

### 2.5. DNA amplification and sequencing

To examine the *OMA1* nucleotide sequence encoding the N-terminal a.a. 122–141, forward primers TCAAGATGCCTCTCAAGTGC and CATTTCTGTAGGACTCTCAAGAA and reverse primer CTGCCCACAATGATAGCAAG were used to amplify 241 and 211 nt, respectively, of Exon 1 of the *OMA1* gene. Reactions included forward and reverse primer pairs, 1 μg of H9c2 total cellular DNA template, dNTPs, Taq polymerase (Roche), and DMSO in 80 μLs total volume. Amplifications were cycled at: 94 °C 1 min, 58 °C 1 min., 72 °C 5 min. for 39 cycles, followed by 72° 10 min. Reactions were checked via 1% agarose gel electrophoresis in 1X TAE buffer. Successful reactions were purified using Roche High Pure PCR Product Purification Kit. Three reactions of each forward/reverse primer pair amplification were sequenced by the University of Chicago DNA Sequencing and Genotyping Facility. Sequence data was compared with the NCBI reference sequence for *R. norvegicus OMA1* (NM_001106669.1).

### 2.6. Gene expression

To analyze gene expression via quantitative reverse transcriptase PCR (qRT-PCR), H9c2 cells grown on 10 cm dishes were processed for total RNA using QIAGEN RNeasy kit, and cDNA prepared using Superscript Reverse Transcriptase (Invitrogen, Carlsbad, CA). The following forward (F) and Reverse (R) primer sets to the indicated *R. norvegicus* mRNAs were used: *ActB*: F: TGTCACCAACTGGGACGATA R: CTTTTCACGGTTGGCCTTAG, *AFG3L2*: F: CTGCCTCCGTACGCTTTATC R: TTCAAATCCTTTGGGAGGTC, *Atp2a2*: F: TACTGACCCTGTCCCTGACC R: ACCATTTCATCCCGGATCTT, *Bak*: F: AAGTTGCCCAGGACACAGAG R: TGTCCATCTCAGGGTTAGCA, *Bax*, F: TGCTAGCAAACTGGTGCTCA R: GGTCCCGAAGTAGGAAAGGA, *Drp1*: F: ATGGCAACATCAGAGGCACT R: ACTACCCTTCCCAATAAGG, *Mybl2*: F: CCACGAGGAGGATGAGCTAC R: CTGGATTCAAAACCCTCAGC, *MyoD*: F: CGTGGCAGTGAGCACTACAG R: TGTAGTAGGCGGCGTCGTAG, *MyoG*: F: TCCAGTACATTGAGCGCCTA R: GCTGTGGGAGTTGCATTCAC, *Myom2*: F: CACAGCGCTTTCATGTTTGT R: GGTGGTTTCCAAGTCACGAT, *Oma1:* F: ATCCTCTAAGCCCTGCTTCC R: GTAACATCCGTCCCCGTATT, *Opa1*: F: CATACTAGGATCGGCTGTTGG R: ACTGTAACACACCCTTTAACT, *p53*: F: CAGTCAGGGACAGCCAAGTC R: GTACCAGGTGGAGGTGTGGA, *Ryr1L*: F: ATACTGTGGAGGCCGGTGTA R: GAGGTGGTGAGGCAACTCAG, *Sln*: F: CTGGAGTTCTCACCCAGACC R: TGGCCCCTCAGTATTGGTAG, *Tnnt2*: F: AGAGGACTCCAAACCCAAGC R: AGTCTGCAGCTCGTTCAGGT, *YME1L*: F: GCTTGTACAGGCAACATCCA R: TCTGTGCTTCTGCTAATCTTTCA. Samples were analyzed via SYBR Green on an Eco Illumina Real-time system (Illumina, San Diego, CA). Expression levels for each were normalized to actin (*ActB*).

### 2.7. Statistical analyses

Each experiment shown in the figures is representative of results obtained in at least three independent experiments (biological replicates) for reproducibility. For ImageJ analyses of OPA1 isoforms, samples were analyzed via one-tailed Student's *t*-test. Data presented are the averaged mean with standard error. For ImageJ analysis of mitochondrial circularity, images were analyzed using one-way ANOVA with Tukey's HSD. Data presented are the average mean with standard error. For comparison of mRNA expression in H9c2s grown in standard versus differentiation media, samples were analyzed via Student's *t*-test. In all experiments and analyses, $P < 0.05$ was considered to be statistically significant. *$P < 0.05$, **$P < 0.01$, and ***$P < 0.001$.

## 3. Results and discussion

### 3.1. Loss of $\Delta\psi_m$ causes mitochondrial fragmentation in H9c2 cardiomyoblasts

CCCP is a protonophore that dissipates $\Delta\psi_m$, causing mitochondrial fragmentation in cultured cells (Legros et al., 2002). Previously, we showed that a threshold of 34% $\Delta\psi_m$, relative to untreated controls, is required for mitochondrial interconnection in 143B osteosarcoma cells (Jones et al., 2017). To explore $\Delta\psi_m$-sensitive mitochondrial dynamics in cardiac-derived cells, H9c2 cardiomyoblasts and control 143B cells were incubated with 10 µM CCCP for 1 h, followed by immunofluorescence to visualize mitochondrial organization. Untreated H9c2s displayed mitochondrial organization of both interconnected reticular and isolated organelles, reflecting a balance of fission and fusion events. In response to challenge with CCCP, the mitochondrial network of H9c2s

was disrupted to a completely fragmented state (Fig. 1A). Similarly, upon CCCP challenge, mitochondria of 143B cells collapsed to a fragmented collection of round organelles (Fig. 1A), consistent with previous results (Jones et al., 2017). Blinded ImageJ quantification of mitochondrial images (Dagda et al., 2009; Garcia et al., 2018) revealed significant increases in mitochondrial circularity for untreated versus CCCP-treated H9c2s ($0.46 \pm 0.02$ versus $0.66 \pm 0.01$) and for control 143Bs ($0.45 \pm 0.02$ versus $0.65 \pm 0.02$) (Fig. 1B), demonstrating mitochondrial fragmentation in both cell lines in response to CCCP. Flow cytometry using tetramethyl rhodamine ester (TMRE) allows monitoring of $\Delta\psi_m$ (Jones et al., 2017; Gilkerson et al., 2012): TMRE fluorescence was significantly decreased in untreated versus CCCP-treated cells of both H9c2s ($10177 \pm 715$ versus $4858 \pm 268$ a.u.) and 143Bs ($4858 \pm 268$ a.u. versus $385 \pm 23$ a.u.) (Fig. 1C), demonstrating dissipation of $\Delta\psi_m$ in both H9c2 cardiomyoblast and 143B osteosarcoma cell lines. These data demonstrate that loss of $\Delta\psi_m$ via CCCP treatment
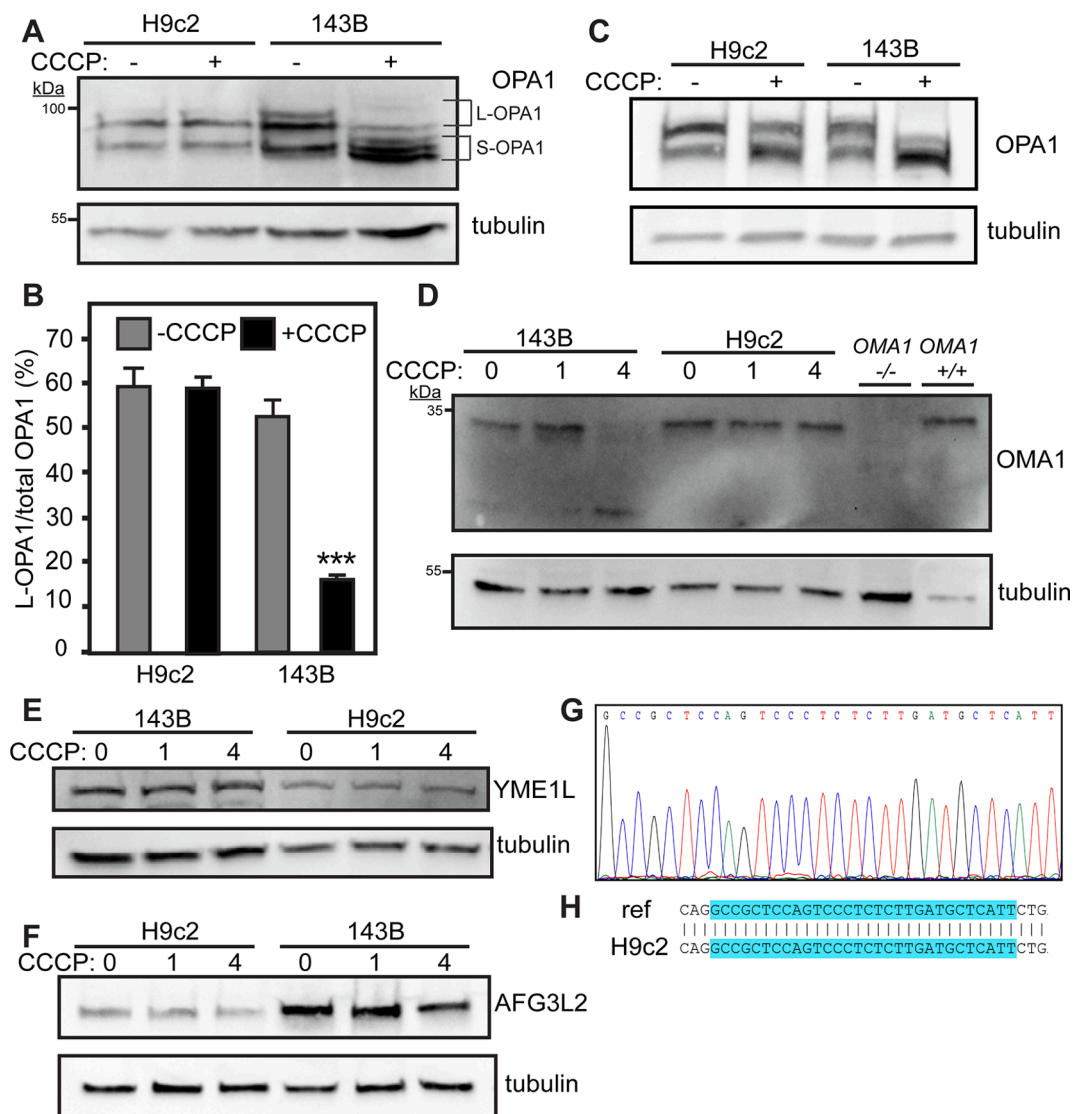


**Fig. 2.** $\Delta\psi_m$-sensitive cleavage of OPA1 is not activated in H9c2 cells. A. H9c2 and 143B cells were challenged with CCCP (10 µM, 1 h) followed by OPA1 immunoblotting. n = 4 experiments (biological replicates). B. ImageJ quantification of L-OPA1 in H9c2s and 143Bs. n = 3 experiments, ± standard error. *** denotes p < 0.001. C. OPA1 immunoblotting of H9c2 and 143B cell lysates following challenge with CCCP (10 µM, 4 h), n = 3 experiments. D. OMA1 immunoblotting of 143B, H9c2 and *OMA1*+/+ and −/− cell lysates treated with 10 µM CCCP for 0, 1, or 4 h, n = 4 experiments. E. YME1L immunoblotting of 143B and H9c2 cell lysates treated with 10 µM CCCP for 0, 1, or 4 h, n = 3 experiments. F. AFG3L2 immunoblotting of 143B and H9c2 cell lysates treated with 10 µM CCCP for 0, 1, or 4 h, n = 3 experiments. G. Representative electropherogram of DNA sequence analysis of *OMA1* nt445-473, encoding the N-terminal $\Delta\psi_m$ sensor domain. Identical results were obtained in sequencing reactions of two independent primer sets, with three amplicons of each sequenced. H. Alignment of reference sequence (ref) NCBI NM_001106669 and H9c2 sequence at nt445-473, indicating no sequence differences (blue).

causes loss of mitochondrial interconnection in H9c2 cardiomyoblast cells, consistent with results in other cellular backgrounds (Legros et al., 2002). We next examined the status of mitochondrial OPA1 in this setting.

### 3.2. L-OPA1 is retained in H9c2s following loss of Δψ$_m$, despite the presence of OMA1

OPA1 is cleaved by the YME1L and OMA1 proteases, creating a steady-state equilibrium of long, fusion-active L-OPA1 and short, fusion-inactive S-OPA1 isoforms (Anand et al., 2014). In response to loss of Δψ$_m$, however, L-OPA1 is typically cleaved to S-OPA1 isoforms (Griparic et al., 2007; Baricault et al., 2007). OPA1 immunoblotting showed that untreated H9c2s maintain steady-state L-OPA1 and S-OPA1 levels. Strikingly, however, under CCCP challenge (10 μM, 1 h), untreated and CCCP-treated H9c2s maintained equivalent proportions of L-OPA1 (Fig. 2A). Conversely, untreated 143B cells maintained a balance of L-OPA1 and S-OPA1, while CCCP induced the expected loss of L-OPA1 and concomitant accumulation of S-OPA1 (Fig. 2A), as shown previously (Jones et al., 2017). ImageJ quantification confirmed that in H9c2s there was no difference in L-OPA1 levels in untreated (59.2 ± 4%) versus CCCP-treated cells (58.9 ± 2%) (Fig. 2B), while untreated 143B cells had significantly greater L-OPA1 than CCCP-treated cells (52.5 ± 4% versus 16.5 ± 0.6%). The CCCP-induced mitochondrial fragmentation in Fig. 1 is surprising in light of the presence of L-OPA1 in H9c2s under CCCP challenge. Notably, OPA1-mediated mitochondrial fusion is opposed by mitochondrial fission, mediated by recruitment of dynamin-related protein-1 (DRP1) to the organelle, where it carries out membrane scission. Mitochondrial recruitment of DRP1 is carried out by the actin cytoskeleton (Ji et al., 2015; Hatch et al., 2014; Moore, 2016) in response to stimuli including AMP kinase (Toyama et al., 2016) and uncouplers (Cereghetti et al., 2008), suggesting that the observed CCCP-induced mitochondrial fragmentation is mediated by DRP1. Moreover, longer incubation with CCCP (four hours) also failed to elicit any appreciable L-OPA1 cleavage (Fig. 2C). These data demonstrate that L-OPA1 is retained under loss of Δψ$_m$ in H9c2s, representing a novel departure from Δψ$_m$-sensitive OPA1 dynamics reported in other cell settings (Griparic et al., 2007; Ishihara et al., 2006; Ehses et al., 2009; Rainbolt et al., 2016).

As Δψ$_m$-sensitive cleavage of L-OPA1 is carried out by OMA1 (Head et al., 2009; Ehses et al., 2009), we next tested whether OMA1 was present in H9c2s. OMA1 immunoblotting of lysates from untreated 143B and H9c2 cells both displayed signal for OMA1, which was missing from control *OMA1*−/− cells (Fig. 2D), demonstrating that the lack of OPA1 cleavage in CCCP-treated H9c2s was not due to the absence of OMA1. In response to loss of Δψ$_m$, OMA1 activates proteolysis of L-OPA1, followed by degradation of OMA1 (Rainbolt et al., 2016; Zhang et al., 2014). While OMA1 was present in untreated 143B cells, 143Bs showed loss of OMA1 signal after 4 h of CCCP treatment, relative to loading controls. Conversely, H9c2s showed no reduction in OMA1 in response to CCCP challenge at 1 or 4 h. (Fig. 2D), indicating that OMA1 activation and degradation did not occur. OMA1 degradation following loss of Δψ$_m$ requires YME1L (Rainbolt et al., 2016), but YME1L is present in both H9c2s and 143Bs without and with CCCP challenge (Fig. 2E). Similarly, the matrix-localized AFG3L2 protease cooperates with YME1L to regulate OMA1 activity (Consolato et al., 2018). AFG3L2 immunoblotting revealed that both H9c2 and 143B cells displayed AFG3L2 signal, though H9c2s displayed less, relative to loading controls (Fig. 2F). Thus, OMA1, and its partners YME1L and AFG3L2, are expressed in H9c2s, but OMA1 is apparently neither activated nor degraded in response to loss of Δψ$_m$.

Langer and co-workers found that a conserved N-terminal domain of OMA1 (a.a. 144–163) is required for its activation and cleavage of L-OPA1 following dissipation of Δψ$_m$ (Baker et al., 2014). To test whether the lack of L-OPA1 cleavage under CCCP challenge in H9c2s (Fig. 2A) might be due to a mutation in the corresponding domain of the rat

*OMA1* gene, we examined the relevant sequence via PCR of isolated H9c2 DNA. The a.a.144–163 domain of human OMA1 corresponds to the rat OMA1 a.a. 122–141, encoded by nt445-473 of the *OMA1* coding sequence. PCR amplification and sequencing of this region (Fig. 2G) demonstrated that this region in H9c2s is identical to the NCBI reference sequence (Fig. 2H), indicating that the observed insensitivity of OMA1 to loss of Δψ$_m$ in H9c2s is not due to mutation or deletion of OMA1′s Δψ$_m$ sensor domain (Baker et al., 2014).

Taken together, these results indicate that L-OPA1 isoforms are retained in H9c2 cardiomyoblasts despite loss of Δψ$_m$, likely through a failure to activate OMA1. *In vivo*, OPA1 plays a key role as an apoptotic switch in cardiac tissue (Wai, 2015). We therefore investigated whether cardiac-like differentiation of H9c2s would potentiate Δψ$_m$-sensitive OPA1 cleavage in this system.

### 3.3. Retinoic acid-mediated differentiation activates L-OPA1 cleavage in H9c2s

H9c2 cells can be induced to differentiate towards skeletal or cardiac muscle phenotypes: when grown in low-serum media, H9c2 cells form myotubes and express skeletal muscle markers, while growth in low-serum media containing RA promotes expression of cardiac markers for a cardiomyocyte-like phenotype (Branco et al., 2015, 2011). To explore the impact of cardiac differentiation on Δψ$_m$-sensitive L-OPA1 cleavage, H9c2s were grown in differentiation media containing 1% FBS with 1 μM RA for 5 days (Branco et al., 2015). When visualized by confocal microscopy, H9c2s grown in standard media (DMEM containing 10% FBS) showed blast-type morphology consistent with actively-dividing cultured cells. When grown in media containing 1% FBS + RA, however, H9c2s transitioned to an elongate cellular morphology, with frequent binucleate cells (Fig. 3A), consistent with differentiation to a more cardiac-like state (Branco et al., 2015). To examine cardiac-specific differentiation, mRNAs were examined by quantitative reverse transcription PCR (qRT-PCR). Strikingly, significant increases in the expression of cardiac-specific genes were observed in differentiated H9c2s: cardiac troponin T (*Tnnt2*, 24-fold), myomesin 2 (*Myom2*, 7-fold), myogenin (*Myog*, 3.5-fold), ryanodine receptor 1 (*Ryr1l*, 4-fold), sarcolipin (*Sln*, 7-fold), and the sarcoplasmic calcium transporter *ATP2a1* (5-fold) all showed significantly increased mRNA expression. Conversely, the *Mybl2* cell cycle progression factor showed decreased expression, while expression of *Myod*, which promotes skeletal (not cardiac) muscle differentiation, was not increased (Fig. 3B). Taken together, these data indicate that H9c2s differentiate upon treatment with low serum plus RA, exiting the cell cycle and committing to a cardiac-specific state. We next examined the effect of RA-mediated differentiation on Δψ$_m$-sensitive OPA1 cleavage in H9c2s.

Following incubation in differentiation media, control and differentiated H9c2s were challenged with CCCP. Undifferentiated H9c2s maintained an average TMRE value of 5881 ± 568 a.u., falling to 1367 ± 542 in response to CCCP for a significant decrease in Δψ$_m$. Differentiated H9c2s had a TMRE value of 6865 ± 292, decreasing to 1998 ± 378 following CCCP treatment (Fig. 3C). Thus, the loss of TMRE in response to CCCP was equivalent in undifferentiated versus RA-differentiated H9c2s. OPA1 immunoblotting revealed that untreated H9c2s had a balance of both L-OPA1 and S-OPA1 isoforms, maintaining L-OPA1 under CCCP challenge, as in Fig. 2. RA-treated H9c2s similarly maintained both L-OPA1 and S-OPA1 isoforms. Strikingly, however, RA-treated H9c2s showed a dramatic loss of L-OPA1 in response to CCCP treatment (Fig. 3D). ImageJ quantification confirmed that while undifferentiated H9c2s showed no difference in L-OPA1 levels (61 ± 4% control versus 56 ± 4% CCCP-treated), RA-differentiated H9c2s showed a robust, significant loss of L-OPA1 in response to CCCP challenge (57 ± 3% control versus 16 ± 5% CCCP-treated) (Fig. 3E). Consistent with this, RA-treated H9c2s maintain interconnected mitochondria, collapsing to a fragmented morphology upon CCCP treatment (Fig. 3F). These results demonstrate that Δψ$_m$-sensitive L-OPA1 cleavage is vigorously activated
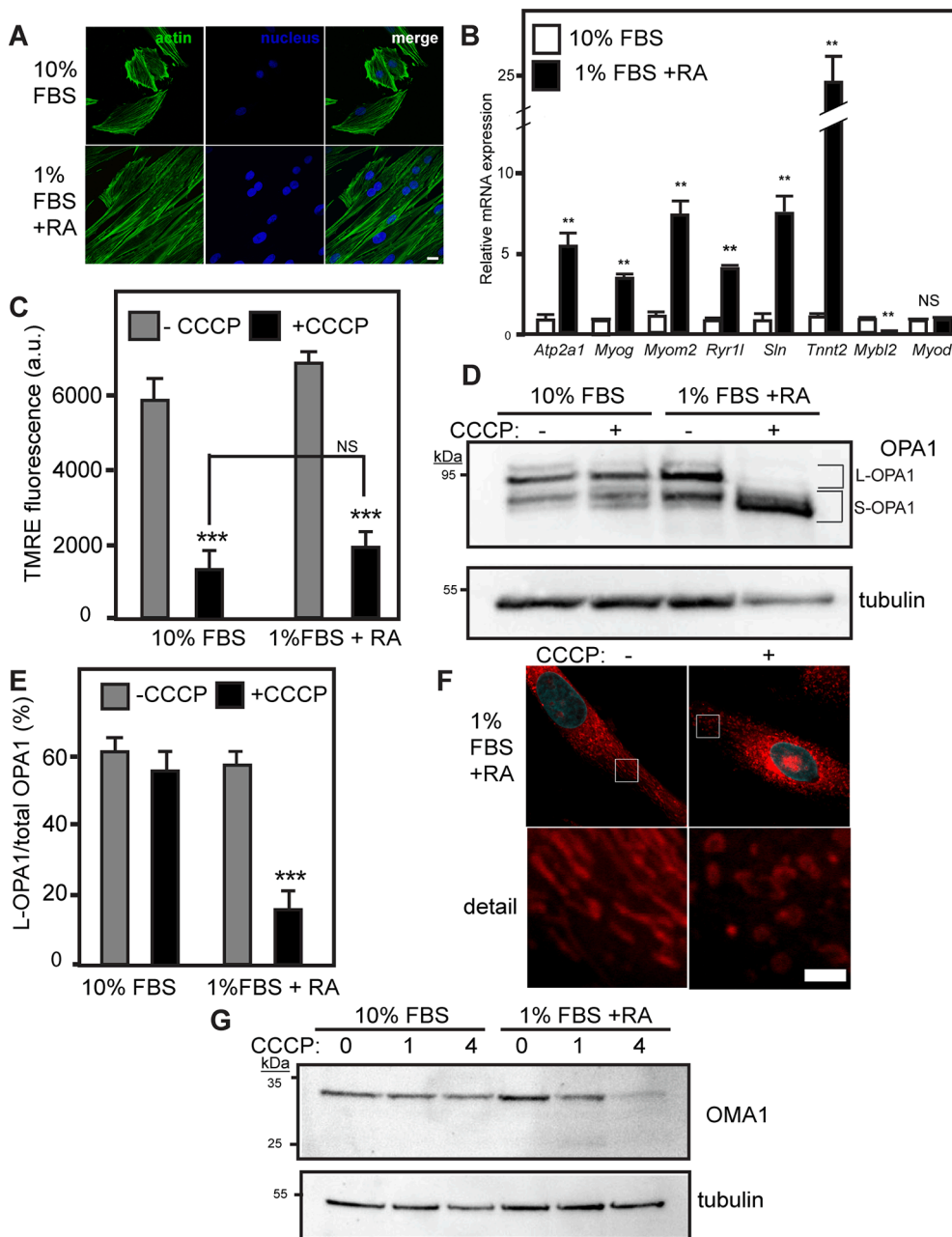
**Fig. 3.** RA-mediated differentiation activates $\Delta\psi_m$-sensitive OPA1 cleavage in H9c2s. A. Confocal imaging of H9c2s grown in standard (DMEM + 10% FBS) or differentiation media (DMEM + 1% FBS + 1 µM RA) for five days. Actin (phalloidin, green), and nuclei (DAPI, blue) were visualized by confocal microscopy. B. Gene expression of differentiation markers in H9c2s in standard (white) or differentiation (black) media. qRT-PCR for indicated mRNAs, ± standard error. ** denotes p < 0.01. C. TMRE flow cytometry analysis for $\Delta\psi_m$ in standard or differentiation media without or with 10 µM CCCP, 1 h. n = 3 experiments. D. H9c2s grown in standard or differentiation media were challenged with CCCP for 1 h followed by immunoblotting for OPA1. E. ImageJ quantification of OPA1 immunoblots. n = 4 experiments, ± standard error. *** denotes p < 0.01. F. Mitochondrial morphology of H9c2s differentiated with 1% FBS + 1 µM RA. Cells were incubated with MitoTracker, followed by CCCP challenge and fixation. Mitochondria (MitoTracker, red) and nuclei (DAPI, blue) were visualized by confocal microscopy. n = 3 expts. G. OMA1 and tubulin immunoblotting of H9c2s grown in standard or differentiation media challenged with 10 µM CCCP for 0, 1, or 4 h, n = 4 experiments. (For interpretation of the references to colour in this figure legend, the reader is referred to the web version of this article.)

in RA-differentiated H9c2 cells. As loss of $\Delta\psi_m$ activates OMA1 cleavage of L-OPA1, followed by subsequent YME1L-dependent degradation of OMA1 (Rainbolt et al., 2016; Zhang et al., 2014), we next examined whether RA differentiation restored degradation of OMA1 following CCCP challenge. In undifferentiated H9c2s, OMA1 was not degraded following CCCP challenge of 1 or 4 h. In RA-differentiated H9c2s, however, CCCP induced loss of OMA1 after 4 h. (Fig. 3G), consistent with CCCP-induced activation and subsequent degradation of OMA1 in RA-differentiated H9c2s. Together, these results demonstrate that RA-mediated differentiation robustly activates CCCP-induced L-OPA1 cleavage, and indicate that $\Delta\psi_m$-sensitive OPA1 cleavage is regulated by a developmental switch in H9c2 cells.

### 3.4. RA-mediated OPA1 cleavage is reversible and chloramphenicol-insensitive

To explore potential mechanisms of this intriguing switch, we examined the mRNA expression of factors involved in mitochondrial dynamics and candidate interacting factors. While RA differentiation did not alter the expression of *OPA1, OMA1, DRP1, YME1L,* or *p53*, RA differentiation caused significant increases in the expression of *AFG3L2* (2-fold) and pro-apoptotic factors *Bax* (1.8-fold) and *Bak* (1.5-fold) (Fig. 4A). As an inhibitor of mitochondrial protein synthesis (Storrie and Attardi, 1973; Hilander et al., 2018), chloramphenicol (CAP) prevents stress-induced OPA1 cleavage in cells with decreased AFG3L2 (Mancini et al., 2019; Richter et al., 2019). To examine whether RA-induced OPA1 cleavage is sensitive to CAP, H9c2s were differentiated for five days, as above, in the absence or presence of CAP for the final three days (Hilander et al., 2018), followed by CCCP treatment. RA-differentiated H9c2s maintain L-OPA1, which is strongly cleaved following CCCP challenge, as above. RA-differentiated H9c2s treated with CAP prior to challenge with CCCP also show complete cleavage of L-OPA1 (Fig. 4B), demonstrating that RA-induced OPA1 cleavage is not CAP-sensitive and indicating that the observed switch is not dependent on mitochondrial
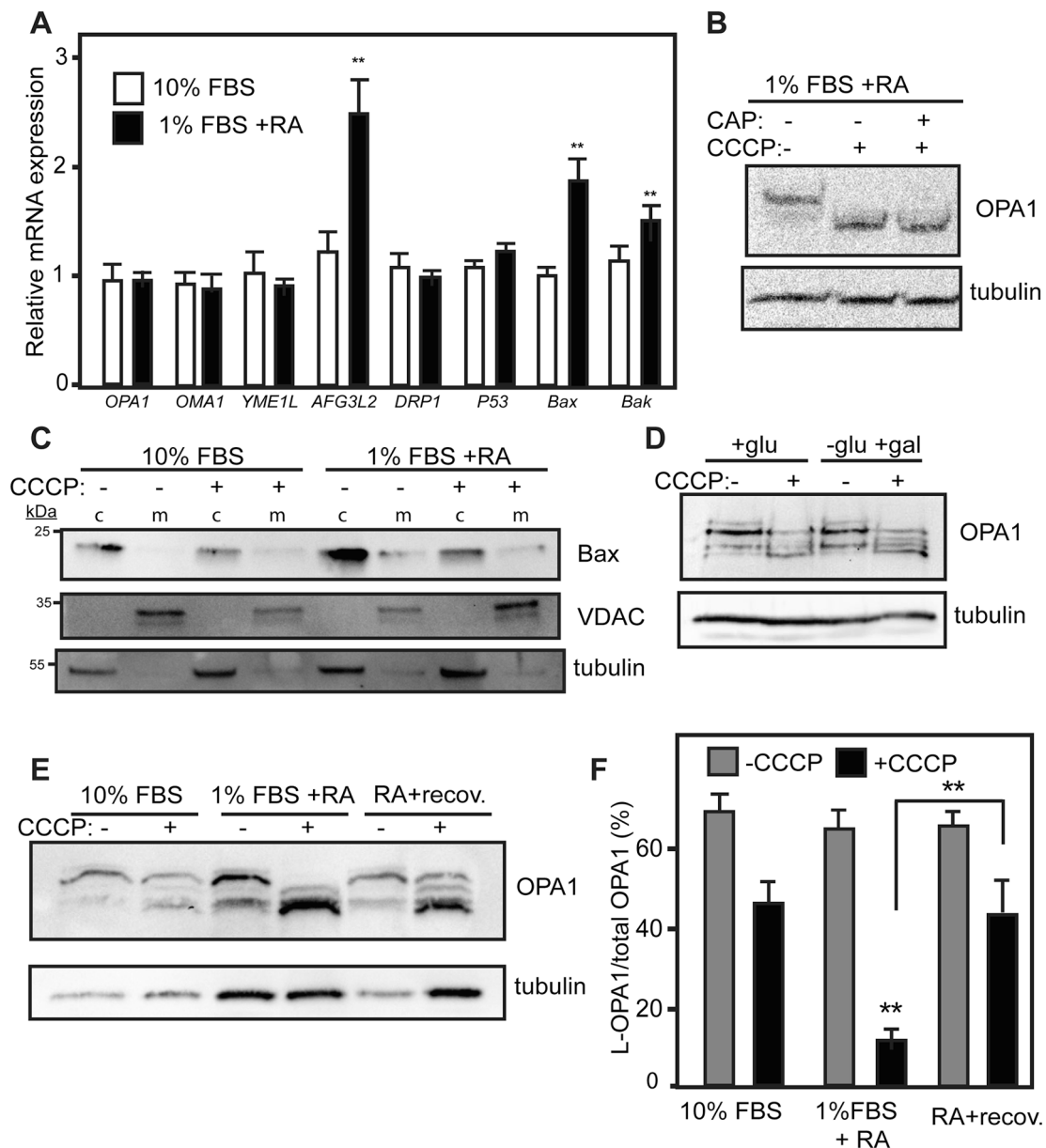
**Fig. 4.** RA-mediated activation of Δψ$_m$-sensitive OPA1 cleavage is reversible, but chloramphenicol-insensitive. A. qRT-PCR of indicated mRNAs from H9c2s grown in standard (10% FBS, white) or differentiation (1% FBS + RA, black) media, ± standard error. ** denotes p < 0.01. B. OPA1 immunoblotting of RA-differentiated H9c2s treated with CAP (40 μg/mL, 3 d) and challenged with CCCP (10 μM, 1 h). n = 3 experiments. C. Immunoblotting of cytosolic (c) and mitochondrial (m) fractions (10 μg per lane) from H9c2s in regular (10% FBS) and differentiation (1% FBS + RA) media, without or with CCCP. n = 3 experiments. D. OPA1 and tubulin immunoblotting of H9c2s grown in glucose (+glu) or galactose (-glu + gal) media and challenged with CCCP (10 μM, 1 h). n = 3 experiments. E. OPA1 and tubulin immunoblotting of cell lysates from 10% FBS, 1% FBS + RA, and RA + recov. H9c2s were differentiated in 1% FBS + RA for 5 d and then allowed to recover for 5 d in 10% FBS (RA + recov.). n = 3 experiments. F. ImageJ quantification of OPA1 immunoblots in E. n = 3 experiments, ± standard error. * denotes p < 0.05, **denotes p < 0.01, ***denotes p < 0.001.

protein synthesis.

Given the increased expression of pro-apoptotic *Bax* and *Bak* in RA-treated H9c2s, we next examined whether Bax is involved in RA-induced OPA1 cleavage. Bax is a cytosolic factor that is translocated to mitochondria in response to a variety of stimuli, where it promotes cytochrome *c* release and subsequent caspase-mediated apoptosis (Eskes et al., 2000; Wolter et al., 1997). Bax and Bak oligomerize within the mitochondria to activate OMA1 (Jiang et al., 2014). To test whether increased mitochondrial translocation of Bax correlates with RA-induced OPA1 cleavage, cytosolic and mitochondrial fractions of control and RA-differentiated H9c2s (without or with CCCP) were prepared. In undifferentiated H9c2s, Bax was predominantly found in the cytosolic fraction, coincident with tubulin. Faint Bax bands were found in

mitochondrial fractions, coincident with mitochondrial voltage-dependent anion channel (VDAC) (Fig. 4C). Similarly, RA-differentiated H9c2s showed strong Bax signal in the cytosolic fractions of control and CCCP-treated cells, with faint bands in the mitochondrial fractions (Fig. 4C). As such, RA differentiation does not appear to cause an appreciable increase in mitochondrial translocation of Bax in response to CCCP.

OPA1 processing is modulated in RPE1 cells by changing from high glucose media to glucose-free media supplemented with galactose (MacVicar and Lane, 2014), thus switching from glycolytic to oxidative metabolism (Rossignol et al., 2004). To test whether OPA1 processing in H9c2s is impacted by metabolic shifting, H9c2s were incubated in DMEM lacking glucose supplemented with galactose, followed by CCCP

challenge. H9c2s grown in high glucose maintain L-OPA1 isoforms, either without or with CCCP challenge (Fig. 4D), as in Fig. 2. Similarly, H9c2s grown in media lacking glucose, supplemented with galactose, retain L-OPA1, even under CCCP challenge (Fig. 4D), indicating that shifting metabolism does not activate OPA1 processing in H9c2s. Consistent with this, RA-mediated differentiation of H9c2s does not significantly alter steady-state $\Delta\psi_m$ of H9c2s (Fig. 3C). Moreover, RA-mediated differentiation is carried out in high glucose media. Taken together, these results suggest that the observed induction of $\Delta\psi_m$-sensitive OPA1 processing in RA-treated H9c2s is not mediated by increased mitochondrial metabolism. We next tested whether RA induction of $\Delta\psi_m$-sensitive L-OPA1 cleavage is reversible. H9c2s were differentiated for 5 days in RA, followed by recovery in media with 10% FBS lacking RA for an additional 5 days. While untreated H9c2s showed no L-OPA1 cleavage in response to CCCP, RA-differentiated H9c2s displayed robust cleavage of L-OPA1 in response to CCCP challenge (as in Fig. 3D). Differentiated H9c2s allowed to recover in DMEM with 10% FBS, however, retain L-OPA1 when challenged with CCCP (Fig. 4E). ImageJ quantification confirms that while H9c2s that recover in standard media do show some reduction in L-OPA1 under CCCP challenge, they retain significantly more L-OPA1 than RA-differentiated H9c2s given CCCP (Fig. 4F). These results demonstrate that the induction of $\Delta\psi_m$-sensitive L-OPA1 cleavage in differentiated H9c2s is reversible upon removal of RA and restoration of serum.

The robust switching of $\Delta\psi_m$-sensitive L-OPA1 cleavage suggests that RA differentiation activates a potent regulatory mechanism for OMA1, opening new avenues of inquiry regarding the mechanistic regulation of $\Delta\psi_m$-sensitive OPA1 cleavage, as well as a novel developmental role for this stress-sensing mechanism. Mechanistically, the stress-sensitive activation of OMA1 remains unclear. Our findings add a provocative new element to this question, suggesting that an unknown, developmentally-regulated molecular 'clutch' is able to engage, and disengage, this key mechanism of mitochondrial stress response. OMA1 interacts with YME1L (Song et al., 2007; Anand et al., 2014; Rainbolt et al., 2016), AFG3L2 (Consolato et al., 2018), and cardiolipin (allowing indirect association with prohibitin (Anderson et al., 2020), suggesting that improved understanding of OMA1′s homo-oligomeric structure (Bohovych et al., 2014), interacting partners, and the inner membrane proteolipid environment will be crucial to fully delineating the mechanisms behind stress-sensitive cleavage of OPA1. Developmental regulation of L-OPA1 cleavage has not been demonstrated previously, despite emerging evidence indicating potent roles for OPA1 in differentiation: ablation of OPA1 disrupts neural (Caglayan et al., 2020) and cardiac development (Kasahara et al., 2013), as well as stem cell maintenance (Sènos Demarco et al., 2019). A developmental switch activating stress-sensitive OPA1 cleavage in differentiated cardiac cells is consistent with OPA1′s established role in priming cells for apoptosis (Head et al., 2009; Jiang et al., 2014) and induction of pro-apoptotic factors in RA-differentiated H9c2s (Fig. 4A; y (Branco et al., 2015). These findings hold exciting potential for other cell settings, including stem, neuronal, and additional cardiac cell systems, in exploring the generality of this intriguing switch.

### Author contributions

R. Gilkerson, I. Garcia, and M. Keniry conceived and designed the experiments. I. Garcia, F. Calderon, P. De La Torre, S. St. Vallier, C. Rodriguez, D. Agarwala, M. Keniry, W. Innis-Whitehouse, and R. Gilkerson performed the experiments. Sequence data was generated by the University of Chicago DNA Sequencing and Genotyping Facility. R. Gilkerson, I. Garcia, and M. Keniry analyzed the data. R. Gilkerson and I. Garcia wrote the manuscript, with contributions from the other authors.

### References

Akepati, V.R., et al., 2008. Characterization of OPA1 isoforms isolated from mouse tissues. J. Neurochem. 106 (1), 372–383.

Anand, R., et al., 2014. The i-AAA protease YME1L and OMA1 cleave OPA1 to balance mitochondrial fusion and fission. J. Cell Biol. 204 (6), 919–929.

Anderson, C.J., et al., 2020. Prohibitin levels regulate OMA1 activity and turnover in neurons. Cell Death Differ. 27 (6), 1896–1906.

Baker, M.J., et al., 2014. Stress-induced OMA1 activation and autocatalytic turnover regulate OPA1-dependent mitochondrial dynamics. EMBO J. 33 (6), 578–593.

Ban, T., et al., 2017. Molecular basis of selective mitochondrial fusion by heterotypic action between OPA1 and cardiolipin. Nat. Cell Biol. 19 (7), 856–863.

Baricault, L., et al., 2007. OPA1 cleavage depends on decreased mitochondrial ATP level and bivalent metals. Exp. Cell Res. 313 (17), 3800–3808.

Bohovych, I., et al., 2014. Stress-triggered activation of the metalloprotease Oma1 involves Its C-terminal region and is important for mitochondrial stress protection in yeast. J. Biol. Chem. 289 (19), 13259–13272.

Branco, A.F., et al., 2011. Isoproterenol cytotoxicity is dependent on the differentiation state of the cardiomyoblast H9c2 cell line. Cardiovasc. Toxicol. 11 (3), 191–203.

Branco, A.F., et al., 2015. Gene expression profiling of H9c2 myoblast differentiation towards a cardiac-like phenotype. PLoS One 10 (6) p. e0129303.

Caglayan, S., et al., 2020. Optic atrophy 1 controls human neuronal development by preventing aberrant nuclear DNA methylation. iScience 23 (6), 101154.

Cereghetti, G.M., et al., 2008. Dephosphorylation by calcineurin regulates translocation of Drp1 to mitochondria. Proc. Natl. Acad. Sci. 105 (41), 15803–15808.

Chen, M., et al., 2016. Mitophagy receptor FUNDC1 regulates mitochondrial dynamics and mitophagy. Autophagy 12 (4), 689–702.

Civiletto, G., et al., 2015. Opa1 overexpression ameliorates the phenotype of two mitochondrial disease mouse models. Cell Metab. 21 (6), 845–854.

Consolato, F., et al., 2018. m-AAA and i-AAA complexes coordinate to regulate OMA1, the stress-activated supervisor of mitochondrial dynamics. J. Cell Sci. 131 (7).

Dagda, R.K., et al., 2009. Loss of PINK1 function promotes mitophagy through effects on oxidative stress and mitochondrial fission. J. Biol. Chem. 284 (20), 13843–13855.

Delettre, C., et al., 2001. Mutation spectrum and splicing variants in the OPA1 gene. Hum. Genet. 109 (6), 584–591.

Ehses, S., et al., 2009. Regulation of OPA1 processing and mitochondrial fusion by m-AAA protease isoenzymes and OMA1. J. Cell Biol. 187 (7), 1023–1036.

Eskes, R., et al., 2000. Bid induces the oligomerization and insertion of bax into the outer mitochondrial membrane. Mol. Cell. Biol. 20 (3), 929–935.

Frezza, C., et al., 2006. OPA1 controls apoptotic cristae remodeling independently from mitochondrial fusion. Cell 126 (1), 177–189.

Garcia, I., et al., 2018. Oxidative insults disrupt OPA1-mediated mitochondrial dynamics in cultured mammalian cells. Redox Rep. 23 (1), 160–167.

Gilkerson, R.W., et al., 2012. Mitochondrial autophagy in cells with mtDNA mutations results from synergistic loss of transmembrane potential and mTORC1 inhibition. Hum. Mol. Genet. 21 (5), 978–990.

Griparic, L., Kanazawa, T., van der Bliek, A.M., 2007. Regulation of the mitochondrial dynamin-like protein Opa1 by proteolytic cleavage. J. Cell Biol. 178 (5), 757–764.

Guillery, O., et al., 2008. Metalloprotease-mediated OPA1 processing is modulated by the mitochondrial membrane potential. Biol. Cell 100 (5), 315–325.

Hatch, A.L., Gurel, P.S., Higgs, H.N., 2014. Novel roles for actin in mitochondrial fission. J. Cell Sci. 127 (21), 4549–4560.

Head, B., et al., 2009. Inducible proteolytic inactivation of OPA1 mediated by the OMA1 protease in mammalian cells. J. Cell Biol. 187 (7), 959–966.

Herkenne, S., et al., 2020. Developmental and tumor angiogenesis requires the mitochondria-shaping protein Opa1. Cell Metab. 31 (5), 987–1003.e8.

Hilander, T., et al., 2018. Analysis of mitochondrial protein synthesis: de novo translation, steady-state levels, and assembled OXPHOS complexes. Curr. Protoc. Toxicol., e56

Ishihara, N., et al., 2006. Regulation of mitochondrial morphology through proteolytic cleavage of OPA1. EMBO J. 25 (13), 2966–2977.

Ji, W.K., et al., 2015. Actin filaments target the oligomeric maturation of the dynamin GTPase Drp1 to mitochondrial fission sites. Elife 4, e11553.

Jiang, X., et al., 2014. Activation of mitochondrial protease OMA1 by Bax and Bak promotes cytochrome c release during apoptosis. Proc. Natl. Acad. Sci. 111 (41), 14782–14787.

Jones, E., et al., 2017. A threshold of transmembrane potential is required for mitochondrial dynamic balance mediated by DRP1 and OMA1. Cell. Mol. Life Sci. 74 (7), 1347–1363.

Kasahara, A., et al., 2013. Mitochondrial fusion directs cardiomyocyte differentiation via calcineurin and notch signaling. Science 342 (6159), 734–737.

Legros, F., et al., 2002. Mitochondrial fusion in human cells is efficient, requires the inner membrane potential, and is mediated by mitofusins. MBoC 13 (12), 4343–4354.

MacVicar, T.D.B., Lane, J.D., 2014. Impaired OMA1-dependent cleavage of OPA1 and reduced DRP1 fission activity combine to prevent mitophagy in cells that are dependent on oxidative phosphorylation. J. Cell Sci. 127 (10), 2313–2325.

Magalhães-Novais, S., et al., 2020. Cell quality control mechanisms maintain stemness and differentiation potential of P19 embryonic carcinoma cells. Autophagy 16 (2), 313–333.

Mancini, C., et al., 2019. Mice harbouring a SCA28 patient mutation in AFG3L2 develop late-onset ataxia associated with enhanced mitochondrial proteotoxicity. Neurobiol. Dis. 124, 14–28.

Merkwirth, C., et al., 2008. Prohibitins control cell proliferation and apoptosis by regulating OPA1-dependent cristae morphogenesis in mitochondria. Genes Dev. 22 (4), 476–488.

Mitra, K., et al., 2009. A hyperfused mitochondrial state achieved at G1-S regulates cyclin E buildup and entry into S phase. Proc. Natl. Acad. Sci. 106 (29), 11960–11965.

Moore, A.S., et al., 2016. Dynamic actin cycling through mitochondrial subpopulations locally regulates the fission-fusion balance within mitochondrial networks. Nat. Commun. 7, 12886.

Olichon, A., et al., 2007. OPA1 alternate splicing uncouples an evolutionary conserved function in mitochondrial fusion from a vertebrate restricted function in apoptosis. Cell Death Differ. 14 (4), 682–692.

Rainbolt, T.K., Lebeau, J., Puchades, C., Wiseman, R.L., 2016. Reciprocal degradation of YME1L and OMA1 adapts mitochondrial proteolytic activity during stress. Cell Rep. 14 (9), 2041–2049.

Richter, U., et al., 2019. Mitochondrial stress response triggered by defects in protein synthesis quality control. Life Sci. Alliance 2 (1).

Rossignol, R., et al., 2004. Energy substrate modulates mitochondrial structure and oxidative capacity in cancer cells. Cancer Res. 64 (3), 985–993.

Sênos Demarco, R., et al., 2019. Mitochondrial fusion regulates lipid homeostasis and stem cell maintenance in the Drosophila testis. Nat. Cell Biol. 21 (6), 710–720.

Song, Z., et al., 2007. OPA1 processing controls mitochondrial fusion and is regulated by mRNA splicing, membrane potential, and Yme1L. J. Cell Biol. 178 (5), 749–755.

Storrie, B., Attardi, G., 1973. Mode of mitochondrial formation in HeLa cells. J. Cell Biol. 56 (3), 833–838.

Toyama, E.Q., et al., 2016. AMP-activated protein kinase mediates mitochondrial fission in response to energy stress. Science 351 (6270), 275–281.

Wai, T., et al., 2015. Imbalanced OPA1 processing and mitochondrial fragmentation cause heart failure in mice. Science 350 (6265) p. aad0116.

Wolter, K.G., et al., 1997. Movement of Bax from the cytosol to mitochondria during apoptosis. J. Cell Biol. 139 (5), 1281–1292.

Zhang, K., Li, H., Song, Z., 2014. Membrane depolarization activates the mitochondrial protease OMA1 by stimulating self-cleavage. EMBO Rep. 15 (5), 576–585.